



The effect of precipitation conditions on the morpho-structural and optical properties of some zinc oxidic based compounds

L. E. Mureşan¹ · I. Perhaiţa¹ · A. M. V. Brânzanic¹ · C. Sarosi¹ · L. Barbu-Tudoran^{2,3} · G. Borodi³ · I. Petean⁴

Received: 7 November 2023 / Accepted: 15 January 2024 / Published online: 3 February 2024

© The Author(s), under exclusive licence to Springer Science+Business Media, LLC, part of Springer Nature 2024

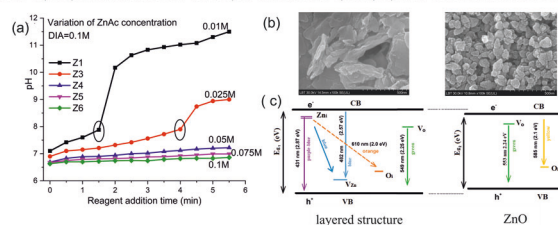
Abstract

Despite the rapid development of a wide variety of materials, zinc oxidic based compounds remain important multifunctional materials. Optimization of synthesis parameters is an essential step in controlling the morpho-structural properties of nanomaterials. For example, preparation of high purity ZnO without additional calcination stage as well as achieving reproducible larger batches is still a great challenge of our days. In this study we report a simple synthesis route for ZnO nanoparticles at room temperature, without any additives and without additional calcination stages using diisopropylamine (DIA) as precipitating agent. The study is focused on changing the molar ratio, the volume and the flow rate of the reactants. Depending on the pH evolution, the phase composition can be controlled to form zinc oxide, zinc hydroxide or layered zinc acetate. Pure zinc oxide phase was obtained at pH ~8 with DIA excess at least of 3 mole. The changes of the morpho-structural and optical properties of samples were investigated by X-Ray diffraction, infrared spectroscopy, scanning electron microscopy, mineralogical optic microscopy, optical and photoluminescence spectroscopy. A better understanding of the crystalline phases formation was achieved using theoretical calculation (DFT) with a good match of the results with the experimental ones. Luminescent studies showed that the emission of ZnO is in green spectral domain at ~548 nm due to $V_O \rightarrow VB$ transitions while the layered zinc acetate exhibits a much more complex blue emission at ~442 and 476 nm due to Zn_i contributions. The luminescent mechanism was proposed, in order to explain the luminescent behavior of samples.

Graphical Abstract

The pH evolution during the precipitation affects the morphology of the samples (layered, rounded aggregates). The blue or green luminescent emission is due to the presence of interstitial zinc (Zn_i) and oxygen vacancies (V_O) in layered zinc acetate or ZnO structures.

Effect of precipitation conditions on the morpho-structural and optical properties of zinc oxidic based compounds



Keywords ZnO · Layered zinc acetate · Precipitation · Luminescence

✉ L. E. Mureşan
laura_muresan2003@yahoo.com

¹ “Raluca Ripan” Institute for Research in Chemistry, Babes-Bolyai University, Fântânele 30, 400294 Cluj-Napoca, Romania

² Electronic Microscopy Centre, Babes-Bolyai University, Clinicilor 5-7, 400006 Cluj-Napoca, Romania

³ National Institute for Research and Development of Isotopic and Molecular Technologies, 65-103 Donath, 400293 Cluj-Napoca, Romania

⁴ Faculty of Chemistry and Chemical Engineering, Babes-Bolyai University, 11 Arany Janos Street, 400028 Cluj-Napoca, Romania

Highlights

- ZnO, Zn(OH)₂ and Zn₅(OH)₈(Ac)₂·4H₂O were prepared by precipitation.
- Preparative parameters were optimized for larger batches of ZnO.
- The phase purity and structural parameters are affected by pH evolution.
- Triangular, rounded, tetragonal bipyramid and lamellar structures were obtained.
- Blue and green luminescence peaked at 442 and 550 nm is due to Zn_i and V_o defects.

1 Introduction

Nanoparticles have gained a lot of attention due to their morphological, textural, and structural properties [1]. ZnO is an excellent multifunctional material, being one of the most produced nano-material along with TiO₂ and SiO₂. Zinc oxide possesses a large band gap energy (3.37 eV), high exciton binding energy (60 meV), and high thermal and mechanical stability at room temperature which makes it suitable for applications in many nanotechnology fields including optoelectronics [2], sensing [3] or catalysis [4]. Moreover, due to its large specific surface area, low toxicity and good biocompatibility, ZnO is used for biomedical applications [5, 6]. Although, ZnO is well studied in terms of its optical, catalytic and electrical properties, researchers still face challenges regarding its morpho-structural control, surface modification and large-scale preparation. Recently, some comprehensive reviews emphasize the importance of optimizing the synthesis conditions in order to control the morpho-structural properties of ZnO [7, 8]. As mentioned in literature, the synthesis of ZnO is performed mainly by: precipitation [9], hydrothermal [10], sol-gel [11], mechanochemical [12], and more recently by green synthesis approaches [13]. Although, each method presents advantages and disadvantages, no technique is better than other since each synthetic route can lead to large varieties of ZnO morphologies which in turn can be correlated to the applicative domain [7]. However, in terms of techniques complexity, the physical methods are expensive and time consuming, requiring high temperature, vacuum, or other critical experimental conditions. When it comes to mass production, it is important to take into account the simplicity of the method, the costs of the reagents, and the energy consumption. Precipitation method is a convenient, facile, and cost-effective approach for the production of ZnO nanoparticles. Generally, the preparation of ZnO nanoparticles implies the reaction between different zinc salts (acetate, chloride, sulfate, nitrate) and basic solutions (containing LiOH, NH₄OH or NaOH) at temperatures between 60 and 90 °C [14, 15]. Since the main component of the precipitation is Zn(OH)₂, the procedure is generally followed by calcination stages up to 600 °C [16, 17] which is an inconvenience in terms of powder morphology and energy consumption. Other methods use microwaves, ultrasounds or high pressure in order to improve the structural composition making the process even more complex [18, 19].

An example is the preparation of ZnO with particles sizes ranging between 29 and 44 nm under supercritical conditions (250–400 °C and 25 MPa) [20]. The mechanism of zinc oxide formation can vary depending on the synthesis condition. Therefore, the increase of pH from 1 to 8 creates a favorable environment to accelerate the hydrolysis and nucleation of ZnO with improved crystallinity [21]. A. Rezaei, and co-authors reported the preparation of different varieties of ZnO (sphere, pyramidal, rod, star, plate) with sizes that decrease from ~1 μm to ~85 nm as the temperature increase up to 70 °C [22].

In our previous study we showed that the preparation of 20 nm sized ZnO for the detection of heavy metals in modified electrodes can be obtained using a facile precipitation route [23]. However, the reproducibility of the product for larger batches is an important issue. We found that repeating the synthesis under the same conditions for larger batches the precipitation was conducted toward the formation of micro-sized Zn(OH)₂ and not toward ZnO. Therefore, the main purpose of this study was to optimize the preparative conditions by varying the molar ratio, volume and flow of the reactants in order to obtain reproducible results. This study brings new insights into the role of pH on the precipitation mechanism as well as on the morpho-structural characteristics of the final products. X-Ray diffraction, infrared spectroscopy, scanning electron microscopy, mineralogical optic microscopy, optical and photoluminescence spectroscopy were used to investigate the structure, shape and size of the particles, and the optical properties of samples. By changing the preparative conditions, the phase composition can be controlled to form zinc oxide, zinc hydroxide or layered zinc acetate. A better understanding of the crystalline phases formation was achieved using theoretical calculation (DFT) with a good match of the results with the experimental ones. The luminescent properties of samples were investigated in detail.

2 Experimental part

2.1 Materials and synthesis procedure

Zinc oxide samples were prepared by precipitation, under well-controlled flow of the precipitating agent in aqueous

medium without addition of any surfactant. Zinc acetate— $\text{Zn}(\text{CH}_3\text{COO})_2 \cdot 2\text{H}_2\text{O}$ (>99.5%, Merck) was used as zinc source and diisopropyl ammine ($\geq 99.5\%$, Sigma Aldrich, *coded DIA*) was used as precipitating agent.

The synthesis consists in the addition of 100 mL solution of DIA with different concentrations at 25 °C into 100 mL zinc acetate solution, under continuous magnetic stirring. The addition of DIA was done at a flow of 18 mL/min using an Heidolph 5201 peristaltic pump. The pH was monitored during the reagent addition. The synthesis conditions and the average pH are presented in Table 1. Larger batches of samples were prepared using the same technique and same preparative conditions but scaled up for volumes of 500 mL. To complete the reaction, the precipitate was allowed to mature for 1 h (aging time). The precipitates were separated by centrifugation, washed twice with double distilled water and dried at 80 °C for 4 h.

2.2 Characterisation of samples

Structure and microcrystalline parameters of samples were evaluated based on X-ray diffraction (XRD) performed using a BRUKER D8 ADVANCE diffractometer with un Ge111 monochromator, in the incident beam at 40 kV and 40 mA, Cu α_1 radiation (1.54056 Å), in the 2θ range $10^\circ \div 80^\circ$. The conversion degree of reagents into ZnO and the presence of various functional groups were evaluated based on the FTIR spectra measured with Nicolet 6700 Spectrometer (KBr pellets technique).

The size and morphology of the samples were revealed by electron microscopy scanning (SEM) using a Hitachi 8230 electron microscope (accelerating voltage of 10 kV). Optical mineralogical microscopy (MOM) was performed for each powder sample, spread it on a glass slide and uniformed onto a thin layer with a spatula. The slides were investigated using a Laboval 2 optical mineralogical microscope, Carl Zeiss Jena, equipped with a digital image capture device Samsung 10 Mpx. The samples were observed firstly in transmitted light and the same area was observed in cross-polarized light, at least three macroscopic areas. The UV-Vis spectra were measured using a double beam UV-VIS Spectrophotometer, Jasco V-750 Able Jasco, with JASCO 150 mm integrating sphere model ILV924, wavelength range 190–900 nm; variable scan speed between $10 \div 4000$ nm/min, scan speed on spectral preview of 8000 nm/min. Luminescent characteristics of samples were evaluated based on emission and excitation spectra registered with Jasco- WAVELL FP-6500 spectrofluorometer, equipped with PMT R928 photomultiplier (glass filter UG1 Reichmann Feinoptik)

2.3 Computational approach

Periodic DFT optimizations of atom positions within fixed unit cells were performed with the aid of the PBE [24] functional at the DND 4.4 effective core [25] basis set level of theory. Dispersion effects were accounted by Grimme's D3 correction [26]. Convergence criteria were set at $2 \cdot 10^{-5}$ Ha for energy, $4 \cdot 10^{-3}$ Ha/Å for forces and maximum

Table 1 Preparative conditions of zinc precursors

Sample code	Precipitation condition*						Type of batch
	ZnAc (M)	DIA (M)	DIA:ZnAc (Molar ratio)	pH _m	pH _f	Flow (mL/min)	
Z1	0.01	0.1	10	9.8	11.5	18	Small
Z2	0.025	0.25	10	8.4	10.6	18	Small
Z3	0.025	0.1	4	7.7	8.9	18	Small
Z4	0.05	0.1	2	7.0	7.2	18	Small
Z5	0.075	0.1	1.33	6.8	6.9	18	Small
Z6	0.1	0.1	1	6.7	6.8	18	Small
Z7	0.05	0.5	10	9.7	11.3	18	Small
Z8	0.075	0.75	10	9.7	11.3	18	Small
Z9	0.1	1	10	10.0	11.4	18	Small
Z10	0.25	1.5	6	8.2	9.6	18	Small
Z11	0.25	0.75	3	7.2	9.0	18	Small
Z12	0.25	0.25	1	6.1	6.8	18	Small
Z13	0.25	0.75	3	10.6	11.4	18	Large
Z14	0.25	0.75	3	8.5	10.6	90	Optimized large

Where: pH_m - the arithmetic average pH during the precipitation; pH_f - the value of pH at the end of the precipitation

* the aging time is 1 h for all samples

displacement was set at $5 \cdot 10^{-3} \text{ \AA}$. All computation were done in DMol3 [27] and computed XRD patterns were performed in Reflex as implemented in Materials Studio 2017 [28].

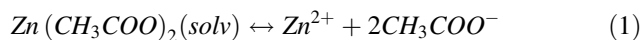
3 Results and discussion

3.1 General characterisation of the precursors

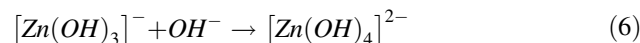
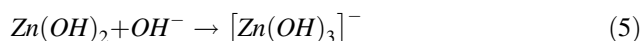
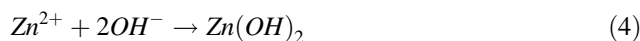
The pH value is a key parameter for the successful preparation of nanomaterials [29]. During the precipitation, the pH may affect the process in multiple ways. If the pH is maintained in the acidic range, the precipitate might be protonated and part of precipitate can be dissolved. At high values of pH, the processes implied in the precipitation may get more complex, due to hydrolysis, condensation of the dissolved species and complexation. Figure 1 presents the evolution of the pH during the precipitation performed in different synthesis conditions.

Analysing the pH values during the precipitation, we can distinguish three main behaviors (Fig. 1). The first pattern is observed for samples prepared using a molar ratio of $\text{DIA:Zn} \leq 2$. In these cases, the precipitation takes place in a slightly acidic media, with no significant pH variations (samples Z4, Z5, Z6, Z12). The second pattern observed for the samples prepared with a high excess of DIA ($\text{DIA:Zn} = 10$) is characterised by an significant increase of pH. The point of the abrupt increase (circle marked) of the pH is associated with the moment of zinc acetate consumption followed by a continuous increase of pH due to the accumulation of DIA in the reaction media (samples Z1, Z2, Z7, Z8, Z9). Finally, the third behavior is met for samples prepared with excess of DIA but maintaining the molar ratio $\text{DIA:Zn} < 10$. In this particular case, an intermediary evolution of pH is observed (samples Z3, Z10, Z11). Depending on the pH, the composition of samples varies from pure ZnO to mixed compounds (as discussed in Section 3.2). Due to large varieties of ionic species formed

between Zn^{2+} and OH^- ions, the formation of ZnO nanoparticles becomes extremely complex and can be described through participation of $\text{Zn}(\text{OH})_2$ or $\text{Zn}(\text{OH})_4^{2-}$ growth units. The formation of zinc oxide can be described by reactions (1–7). Firstly, in zinc acetate aqueous solution, an equilibrium between its corresponding ions takes place according to the reactions (1–2). Furthermore, DIA acts as a strong base, due to inductive effect of alkyl group, accepting H^+ , using the electron pair from nitrogen and therefore, producing the hydroxyl anions as described in reaction (3).



As a result of OH^- production, the nucleophilic attack initiates the formation of ZnO nanoparticles by several hydrolysis and condensation processes of the dissolved species according to reactions (4–7):



At higher concentration of DIA ($\text{DIA:Zn} = 10$) the pH increase significantly after the first minute of precipitation, therefore higher-order of zinc hydroxo-complexes are formed and higher amount of ZnO is formed accordingly. XRD results confirm that precipitation performed at molar ratio of $\text{DIA:Zn} = 10$ leads to ZnO - $\text{Zn}(\text{OH})_2$ mixtures with higher proportion of ZnO. Literature also mention an increased transformation of $\text{Zn}(\text{OH})_2$ toward ZnO as the pH increases [30]. On the contrary, if the acetate concentration

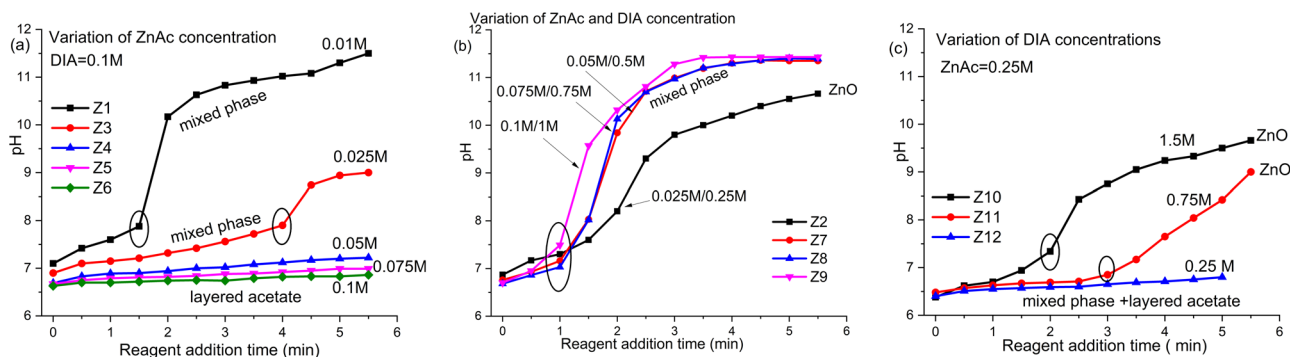


Fig. 1 Evolution of pH during the precipitation by varying the concentration of ZnAc (a); ZnAc - DIA (b); DIA (c), and the phase composition related to each synthesis

is higher, $\text{Zn}(\text{OH})^+$ is produced since DIA cannot supply enough OH^- for the $\text{Zn}(\text{OH})_2$ formation. Moreover, due to the acidic media, part of $\text{Zn}(\text{OH})_2$ is re-dissolved due to its instability and zinc acetate with layered structures are obtained. For samples Z10, Z11 (DIA:Zn = 3 or 6) the increase pH up to ~ 9.5 takes place progressively, providing a better control on the nucleation-aging process, conducting toward the formation of pure ZnO (confirmed by XRD).

3.2 Structural characterization of samples by XRD and FTIR

The XRD patterns of samples prepared in smaller batches are presented in Fig. 2, while for larger batches are depicted in Fig. S1a, c (Supplementary material-SM). Depending on the synthesis conditions, one can see the presence of ZnO, $\text{Zn}(\text{OH})_2$ and layered zinc acetate (ZnAc) phases. Based on X-ray diffractograms, the samples can be classified as follows: (1) pure ZnO samples (Z10, Z11, Z2); (2) mixed samples containing ZnO and $\text{Zn}(\text{OH})_2$ in variable proportions (Z3, Z7, Z8, Z9, Z1, Z12) and (3) layered zinc acetate containing samples (Z4, Z5, Z6). We also found that, the flow and volume of reagents are important parameters in obtaining pure ZnO (Fig. S1a, b). $\text{Zn}(\text{OH})_2$ was obtained in synthesis with larger volume of reagents (500 mL) using the same conditions as for 100 mL. However, the increase of the reagents flow rate from 18 mL/min to 90 mL/min led to pure ZnO phase.

The diffraction peaks at 31.53° ; 34.01° and 36.07° that corresponds to (110), (002), (101) planes, match well with the standard XRD data of ZnO indexed to hexagonal wurtzite structure, space group $\text{P6}_3\text{mc}$ with the cell

parameters: $a = 3.249 \text{ \AA}$, $c = 5.206 \text{ \AA}$ (JCPDS 89-7102). The $\text{Zn}(\text{OH})_2$ phase with the main diffraction peaks at 20.24° ; 20.95° , 27.24° , 27.83° , and 32.92° corresponding to (011), (002), (012), (102) (112) planes belongs to the orthorhombic system, with the space group $\text{P2}_1\text{2}_1\text{2}_1$, and lattice parameters $a = 4.905 \text{ \AA}$, $b = 5.143 \text{ \AA}$ and $c = 8.473 \text{ \AA}$ (JCPDS 89-0138). New diffraction lines are observed in the range $4 - 20^\circ$, such that XRD patterns of Z4, Z5, Z6 show a symmetric sharp reflection at 6.65° and a weak asymmetric reflection at higher angle degree (33.2°) which are in concordance with results reported in literature for layered structure of $\text{Zn}_5(\text{OH})_8(\text{Ac})_2 \cdot 4\text{H}_2\text{O}$ [31, 32].

The crystallites sizes were calculated based on Scherrer's formula $D_{\text{eff}} = k\lambda/\beta\cos\theta$ (where, D_{eff} is the crystallite size (nm)), k is geometrical factor, λ is the X-ray wavelength (Cu K α ; 1.5405 \AA), β is the full width at half maximum (FWHM in radians corrected by instrumental broadening), θ is the Bragg's angle in degrees. The maximum line diffraction for ZnO (101) and $\text{Zn}(\text{OH})_2$ (011) was chosen for calculation. The samples with the smallest crystallite sizes are those containing pure ZnO samples, namely: Z10 (24.6 nm); Z11 (27 nm) and Z2 (26.3 nm). Crystallite sizes for layered zinc acetate are as follows: 65.8 nm (Z4); 87 nm (Z5) and 53 nm (Z6) while the phase composition and crystallite size of samples containing ZnO - $\text{Zn}(\text{OH})_2$ mixture is shown in Table 2. The phase composition of samples was determined using the Reference Intensity Ratio (RIR) methodology [33] based on the equations: $(I_{\text{ZnO}} / I_{\text{Zn}(\text{OH})_2}) = (C_{\text{ZnO}} / C_{\text{Zn}(\text{OH})_2}) \cdot (X_{\text{ZnO}} / X_{\text{Zn}(\text{OH})_2})$ and $X_{\text{ZnO}} + X_{\text{Zn}(\text{OH})_2} = 1$, were: I_{ZnO} , $I_{\text{Zn}(\text{OH})_2}$ - the intensity of the most intense diffraction lines from the ZnO and $\text{Zn}(\text{OH})_2$

Fig. 2 XRD patterns spectra of ZnO sample prepared with 0.1 M DIA and different ZnAc concentrations (a) and different DIA and ZnAc concentrations (b)

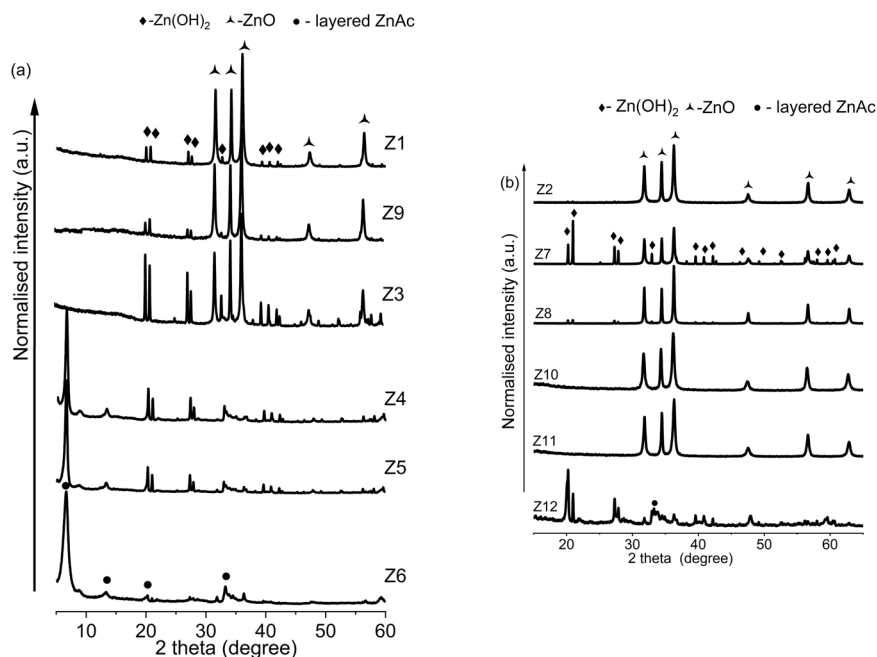


Table 2 Structural phase and crystallite sizes of samples prepared in different synthesis conditions

Sample code	Phase composition (%)			Cristallite size (Å)			pH _f	DIA:ZnAc (Molar ratio)
	ZnO	Zn(OH) ₂	Zn ₅ (OH) ₈ (Ac) ₂	ZnO	Zn(OH) ₂	Zn ₅ (OH) ₈ (Ac) ₂		
Layered zinc acetate samples								
Z4	–	–	Main phase ^a	–	–	65.8	7.2	2
Z5	–	–	Main phase ^a	–	–	85.0	6.9	1.33
Z6	–	–	Main phase ^a	–	–	53.0	6.8	1
Z12 ^b	9	91	Neglected ^a	29.8	40.5	–	6.8	1
Pure ZnO samples								
Z10	100	0	0	24.6	–	–	9.6	6
Z11	100	0	0	27.0	–	–	9.0	3
Z2	100	0	0	26.3	–	–	10.6	10
Mixed ZnO - Zn(OH) ₂ samples								
Z3	51	49	0	41.8	81.0	–	8.9	4
Z1	80	20	0	31.2	79.0	–	11.1	10
Z7	49	51	0	20.0	135.0	–	11.3	10
Z8	91	9	0	26.4	115.8	–	11.3	10
Z9	83	17	0	30.9	81.0	–	11.4	10

Where: ^avalue not calculated because Zn₅(OH)₈(Ac)₂ is not indexed in the PDF database;

^bThe phase composition of Z12 is calculated by neglecting Zn₅(OH)₈(Ac)₂ phase; pH_f - the value of pH at the end of the precipitation

phase, C_{ZnO} , $C_{\text{Zn(OH)}_2}$ - corundum factors for the ZnO and Zn(OH)₂ phase; X_{ZnO} , $X_{\text{Zn(OH)}_2}$ -the mass concentrations of the ZnO and Zn(OH)₂ phase.

Based on the XRD results, it is clear that the molar ratio or reagents as well as the pH play an important role on the precipitation processes affecting the phase composition. An optimal DIA:Zn ratio is mandatory to obtain pure ZnO (Z10, Z11) while an insufficient DIA amount decreases the ZnO content up to 9.1% (Z12) due to re-dissolving of zinc species in the acidic precipitation medium.

Further, if the molar ratio DIA:Zn is kept at 10, the pure ZnO formation does not occur without an optimal concentration of the reactants (i.e. 0.25 M ZnAc and 0.25 M DIA for Z2 sample). As the concentration of zinc acetate increases from 0.01 M (Z1) to 0.025 M (Z3) the Zn(OH)₂ phase increase from 20% (Z1) to 49% (Z3) confirmed also by the increase of diffraction lines. On the other hand, increasing the zinc acetate from 0.01 M to 0.1 M affects the precipitation equilibrium toward the formation of zinc basic acetate (Z4, Z5, Z6) which possess similar structure with layered zinc hydroxy nitrate [32]. The formation of stable Zn₅(OH)₈(NO₃)₂(H₂O)₂ in slightly acidic solution (pH~6) is mentioned in the literature [34] therefore, in our case the formation of zinc hydroxy acetate variety is expected for samples Z4, Z5, Z6 as long as the pH is maintained in acidic range (pH~6).

The most intense peak at 6.65° suggests an interlayer d-spacing of 1.33 nm, corresponding to the (001) diffraction planes of the layered structure composed of positively charged

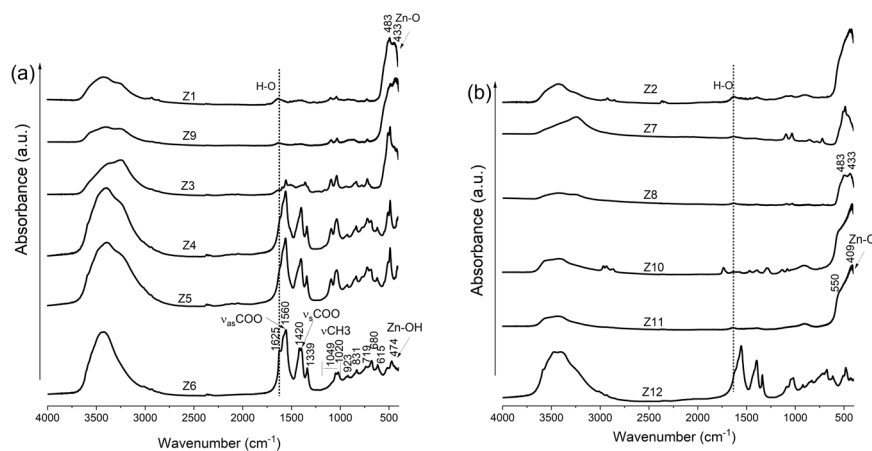
complex $[\text{Zn}_5(\text{OH})_8(\text{H}_2\text{O})_2]^{2+}$ and interlayer anionic species (CH₃COO⁻). Supplementary peak at 33.2° (d = 0.27 nm) continued with a shoulder peak corresponds to the (100) plane from the intermediate layer presented between the ordered zinc hydroxide layers. In the literature there are no crystallographic data on layered zinc acetates. The study with available crystallographic data is only for Zn₅(OH)₈(NO₃)₂·2H₂O single crystal with layered structure [35]. This structure is described like brucite type $[\text{Zn}_3(\text{OH})_8]^{2-}$ layers with nitrate groups located between the sheets, bonded through hydrogen bonding to two water molecules of one layer and an OH⁻ group of the different layers. FTIR was used as a complementary technique to reveal the functional groups in the samples as well as to evaluate the conversion degree of starting reagents into zinc oxide. Firstly, the FTIR spectra of starting reagents were measured and the spectra are shown in Fig. S2 (SM). After the completion of precipitation, the samples composition changes significantly as depicted in Fig. 3.

At low concentration of zinc acetate, the FTIR spectra are dominated mainly by the vibrational bands situated at 483, 433 and 409 cm⁻¹, assigned to Zn-O vibration which are indicators of the zinc hydroxide or zinc oxide presence.

The band located at 717 cm⁻¹ is related to δOH groups while, the two bands at 1027 and 1051 cm⁻¹ describe the asymmetric stretching vibrations of Zn-O-Zn bridge oxygen in the structure [36].

As the concentration of zinc acetate increases from 0.01 M up to 0.1 M, new bands appear at ~1560, ~1420, ~1339 cm⁻¹, which are assigned to asymmetric and

Fig. 3 FTIR spectra of ZnO sample prepared with different concentrations of ZnAc (a) and DIA (b)



symmetric COO^- vibrations from the acetate fragments. Bands in the range $600\text{--}1020\text{ cm}^{-1}$ are related to C-H rocking vibration, C-C stretching vibration, O-C-O bending mode, and COO^- rocking vibration modes [37]. Comparing the FTIR spectra of samples Z4, Z5, Z6, and Z12 with those of the starting reagents, are observed small shifts of the vibrations as well as apparition of new bands (bullet marked in Fig. S2, SM) which confirm the formation of basic zinc acetate compounds. The water bending vibration mode expected to appear at $\sim 1620\text{ cm}^{-1}$ in basic zinc acetate complex is clearer seen in samples Z6 and Z12. C-H symmetric and asymmetric stretching vibration bands of the interlayer acetate anion are observed at $\sim 2900\text{ cm}^{-1}$ [32].

3.3 DFT analysis of samples

Periodic DFT calculations were performed on the crystal structures of ZnO and $\text{Zn}(\text{OH})_2$ compounds in order to test the performance of our DFT methodology. The results are presented in Fig. S3 (SM) and they show a good agreement with the experimental results. In addition, they are in agreement with the structural information (i.e. geometry, XRD) found on their entries in the Materials Project database [38].

For a better understanding of our experimental results regarding the layered compound, the Stahlin $\text{Zn}_5(\text{OH})_8(\text{NO}_3)_2 \cdot 2\text{H}_2\text{O}$ structure was used as starting point to model the structure for our layered $\text{Zn}_5(\text{OH})_8(\text{CH}_3\text{COO})_2 \cdot 2\text{H}_2\text{O}$ compound. In doing this, the NO_3 fragment was replaced by acetate (CH_3COO^-) and the size of the unit cell was modified in order to better adjust the larger CH_3OO^- molecule. The adjustment was done by interpreting the peak found at $2\Theta = 6.65^\circ$ as a reflection caused by the Zn-Zn interlayer separated by a distance $d_{\text{Zn-Zn}} = 13.3\text{ \AA}$. The DFT optimized $\text{Zn}_5(\text{OH})_8(\text{CH}_3\text{COO})_2 \cdot 2\text{H}_2\text{O}$ structure is depicted in Fig. S4 with the fractional coordinates of its constituting atoms being collected in Table S1 (SM). Being a double layered structure, the unit cell possesses two $d_{\text{Zn-Zn}} = 13.3\text{ \AA}$

gaps between the three layers of Zn chains as depicted in Fig. S4a.

Therefore, the unit cell lattice parameter along this direction is accounted by the two $d_{\text{Zn-Zn}}$ gaps, i.e. $a = 26.6\text{ \AA}$. As expected, $d_{\text{Zn-Zn}}$ and ‘a’ values are smaller in the Stahlin structure since the anion species (NO_3^-) fixed between the Zn layers is shorter (Table S2) than the acetate moiety expected to be present between the Zn layers of Z6. The peaks found at $2\Theta = 13.3^\circ$ and $2\Theta = 20.7^\circ$ in the XRD data of Z6 are interpreted as reflections caused by the unit cell’s *b* and, respectively, *c* lattice parameters possessing the corresponding *d* values associated with these 2Θ angles, $b = 6.6\text{ \AA}$ and $c = 4.4\text{ \AA}$. The space group and lattice angles of the Stahlin structure were preserved, i.e. the C2/M space group and lattice angles $\alpha = \beta = \gamma = 90^\circ$. Acetate rotation within the cell was determined by computing XRD spectra of both possible orientations and choosing the one that better reproduced the experimentally observed peaks from Fig. 3.

The computed XRD spectrum matches to a high degree the experimental XRD spectrum of sample Z6 as depicted in Fig. S4b. Besides, the expected peaks $2\Theta = 6.65^\circ$, 13.3° and 20.7° that were used to construct the model, the positions of several other experimental peaks are reproduced by our model (such as $2\Theta = 21.3^\circ$, 24.5° , 26.3° , 27° , 33.8° , 39.7°), albeit intensities are less accurate reproduced.

This suggests that the DFT computed atomic positions (which influence the intensity of reflections) are only to a certain extent in agreement with the actual positions of atoms within Z6 unit cell. However, the lack of experimental data regarding the $\text{Zn}_5(\text{OH})_8(\text{CH}_3\text{COO}^-)_2 \cdot 2\text{H}_2\text{O}$ structure (i.e. single-crystal XRD) prohibits the further adjustment of our model and therefore the obtained structure is used for the frequency analysis yielding the (DFT computed) IR spectrum (Fig. S5–SM).

Overall, DFT overestimates the positions of IR values in the range of hundreds of cm^{-1} , which does not come as a surprise considering the fact that, in general, standard DFT

methods do not reach chemical accuracy (i.e. energy errors in the range $1\text{--}2\text{ kcal/mol} = 350\text{--}700\text{ cm}^{-1}$). For instance, DFT finds the OH bending vibration of H_2O at 1771 cm^{-1} , which is with 146 cm^{-1} above the experimental value. Nevertheless, when adjusting for this overestimation, the computed values correlate with the positions of the experimental values and also, as emphasized in Figs. S6–S14 (SM), the nature of the found vibrations correspond to the experimentally determined counterparts.

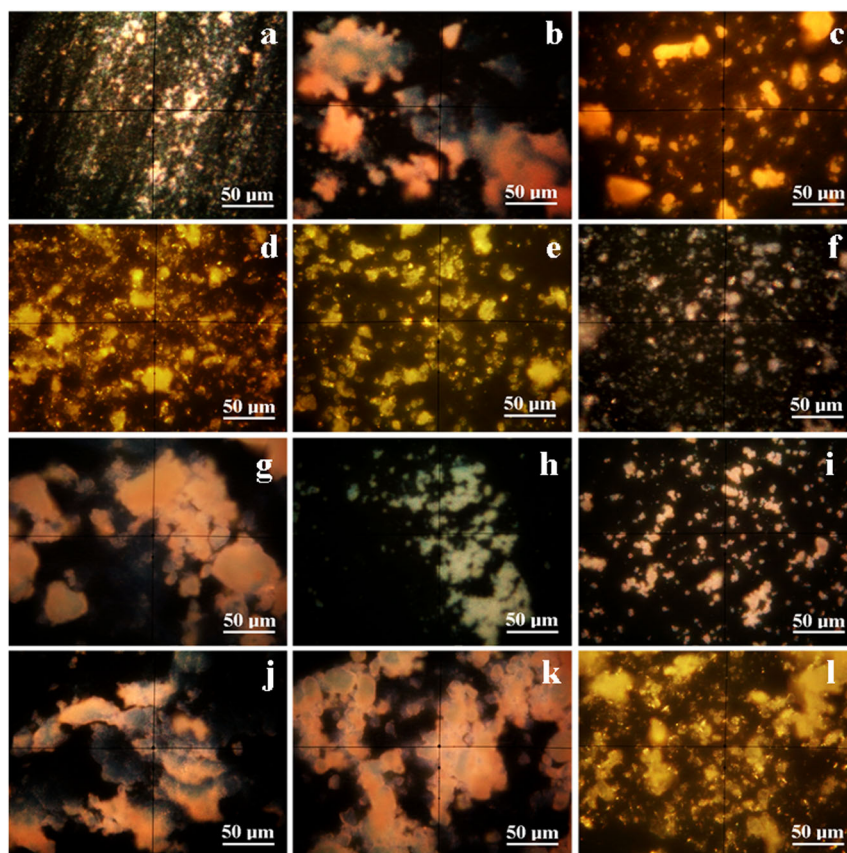
3.4 Mineralogical and morphological characterization by MOM and SEM

Mineralogical optical microscopy (MOM) in cross polarized light allows a proper correlation between cluster shape and color with the phases identified by XRD. Low and high magnification images are presented in Fig. S15 (SM) and Fig. 4, while the transmitted light microscopy images of the same area observed in cross-polarized light are presented in Fig. S16 (SM). MOM image of Z1 shows a uniform thin layer of powder consisting from small fractions with sizes ranging from 0.5 to $3.5\text{ }\mu\text{m}$ (Fig. 4a). The complex morphology derives from polyhedral shape combined with rounded corners, randomly oriented. The observed color is a combination of brown-orange corresponding to ZnO and yellow

corresponding to $\text{Zn}(\text{OH})_2$ [39–41]. MOM image of Z9 (Fig. 4b) reveals cloudy microstructural domains ranging from 10 to $100\text{ }\mu\text{m}$, brown—orange colored with a slightly influence of yellow suggesting a higher content of ZnO in concordance with XRD results (Table 2, Fig. 2b). The $\text{Zn}(\text{OH})_2$ amount progressively increases in Z3, (Fig. 4c), tendency that is continued in sample Z4 (Fig. 4d). Moreover, for Z4, a bright yellow characteristic nuance with goldish spots is observed due to lamellar structure of layered zinc acetate phase. Sample Z5 presents a pronounced yellow nuance due to the significant amount of $\text{Zn}(\text{OH})_2$ and to the increasing of layered ZnAc phase content which dominates the small nanoparticles clusters with sizes between 10 and $40\text{ }\mu\text{m}$ (Fig. 4e). The layered ZnAc amount increases severely in Z6 (Fig. 4f) and combined with disappearance of $\text{Zn}(\text{OH})_2$ phase generate a uniform color nuance of pale yellow with local bright spots. The color extinction phenomenon observable as a brown orange colored with darkened blue nuance for Z10, Z11, Z2 samples, is related to the high purity ZnO phase (Fig. 4j, k, g).

Sample Z8, (Fig. 4i) presents rounded nanoparticles clusters ($0.5\text{--}5\text{ }\mu\text{m}$) with brown orange color with slightly yellow influence due to the low amount of $\text{Zn}(\text{OH})_2$. Samples Z7 and Z12, dominated by zinc hydroxide presence, exhibit pale-yellow appearance (Fig. 4h, l). Moreover, due to some bright yellow spots observed (Fig. 4l), layered

Fig. 4 MOM images of ZnO samples observed in cross polarized light—high magnification ($\times 1200$): (a) Z1, (b) Z9, (c) Z3, (d) Z4, (e) Z5, (f) Z6, (g) Z2, (h) Z7, (i) Z8, (j) Z10, (k) Z11, and (l) Z12



ZnAc might be present in Z12 in good agreement with XRD results.

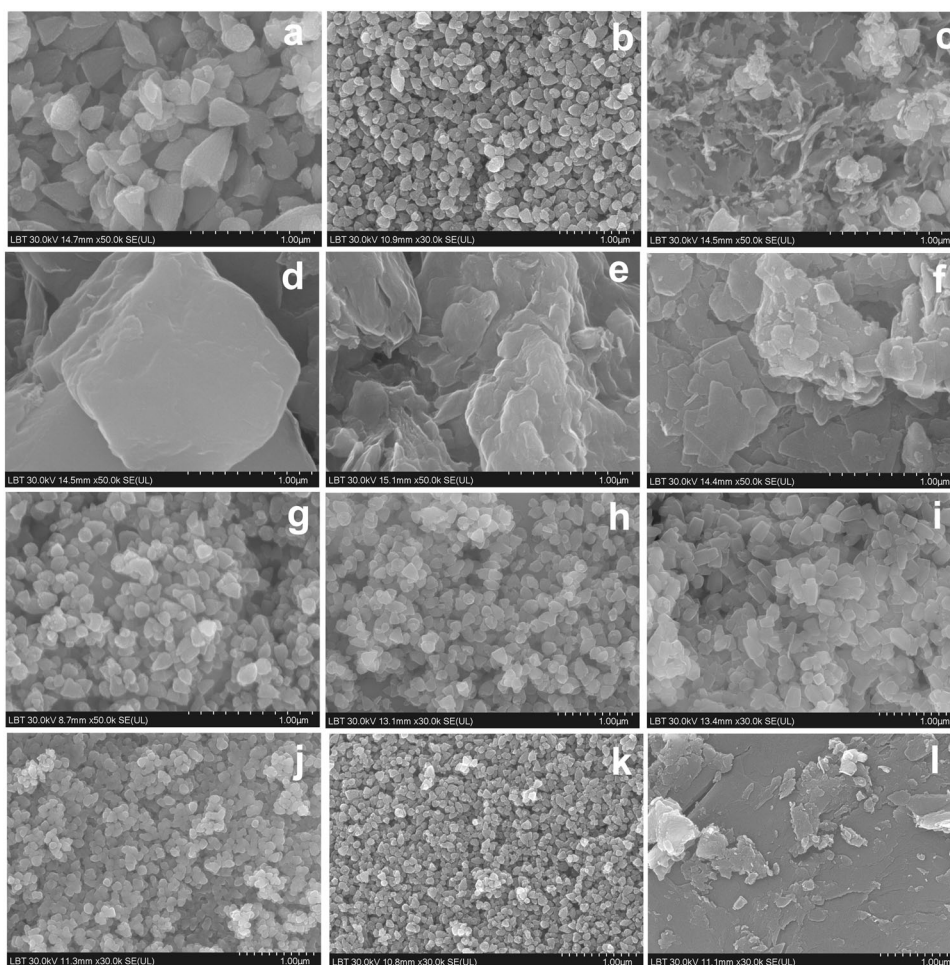
SEM images depicted in Fig. 5 and Fig. S1b, d show different types of morphological structures obtained in different synthesis conditions. Firstly, Z1 consist of triangular aggregates with sizes between 200 and 625 nm, randomly distributed (Fig. 5a). Increase of the reagents concentration by ten times significantly decrease the aggregates sizes (Z9) in the range of 100–150 nm (Fig. 5b), while decrease of the DIA:Zn molar ratio from 10 (Z1, Z9) to 4 (Z3) leads to formation of flaky aggregates of ~ 200 nm (Fig. 5c). Further changes in morphology are observed with the increase of zinc acetate concentration as result of layered zinc acetate phase presence. For example, Z4, consists of platelet aggregates with an almost rectangular polyhedral shape (~2 μm) and thickness between 30 and 150 nm and composed by successive nanostructured layers of sizes between 40 and 80 nm (Fig. 5d).

According to the XRD, the layered zinc acetate content increases progressively from Z4 to Z6 simultaneously with the decrease of $\text{Zn}(\text{OH})_2$. The SEM images (Fig. 5e, f) highlight this phenomenon through the progressive shredding of the

particles as well as with fragmentation of the layers at sizes between 55 and 85 nm. As a result of fragmentation (Z6), platelets become predominantly submicron sized (150 - 600 nm) with a relatively square shape. Sample Z12 has a complex structure based on $\text{Zn}(\text{OH})_2$ clusters with a rocky appearance in a wide range of sizes (50 nm–1 μm) without excluding the existence of larger formations (5 μm).

There are also relief curves that indicate the moderate presence of the layered structure. As for the purest ZnO samples (Z2, Z10, Z11) the SEM images (Fig. 5g, j, k) shows submicron rounded aggregates with sizes that decreases from ~270 nm (Z2) to ~100 nm (Z11). Sample Z13, prepared in large batch with 18 mL/min, presents as tetragonal bipyramids of ~4.5 μm (Fig. S1b) while optimized Z14 prepared in large batch but with 90 mL/min (Fig. S1d) shows a similar morphology with Z11, consisting in rounded nano-aggregates with average size of 130 nm. As a general remark, depending on the synthesis conditions, two types of morphology were identified, rounded aggregates and lamellar morphology with plate-like particles, depending on the phase composition (ZnO , $\text{Zn}(\text{OH})_2$, layered ZnAc).

Fig. 5 SEM images of samples ZnO prepared in different synthesis conditions: (a) Z1, (b) Z9, (c) Z3, (d) Z4, (e) Z5, (f) Z6, (g) Z2, (h) Z7, (i) Z8, (j) Z10, (k) Z11, and (l) Z12



3.5 Optical characterization of samples

Representative diffused reflectance spectra are depicted in Fig. 6a. In the range of 250–350 nm are identified three reflections at 220 nm (5.63 eV); ~258 nm (4.80 eV), and ~352 nm (3.52 eV).

Although the reflectance spectra have a similar appearance, two trends can be observed depending on the crystallographic composition of the samples. A low reflectance, in the range of 250–365 nm, is obtained for samples with ZnO as main phase, and a significantly increase of reflectance appears in case of samples containing layered zinc acetate. Sample Z3 exhibits the lowest optical response under the UV-vis light irradiation. The energy band gap of samples was estimated from diffused reflectance spectra using Kubelka Munk method [42]. For band gap calculations, the Kubelka Munk factor, $F(R)^2$ was plotted as the function of energy as depicted in Fig. 6b. The bandgap reported in literature for $Zn(OH)_2$ and for ZnO is 2.98 eV [43] and 3.33 eV [44] respectively. In our case, the band gap of the samples varies between 3.26 eV and 3.31 eV.

The excitation (PLE) and emission (PL) spectra of samples prepared in different synthesis conditions are depicted in Fig. 7. The excitation spectra (Fig. 7a, c), measured at the maximum of the emission, present a single asymmetrical broad band in the range of 300–400 nm with maxima at 361 nm and a FWHM of 44.66 nm (Z10) and 36.79 nm (Z11).

Presence of $Zn(OH)_2$ as a secondary crystallographic phase (Z7, Z8) broadens the excitation spectrum with apparition of a shoulder at 368 nm and a FWHM of 47.4 nm (Z7) and 43.4 nm (Z8). The asymmetrical shape clearly indicates the presence of various intra-gap defect states. Presence of layered zinc acetate (Z4, Z5, Z6) generates a splitting of the excitation band into two broad bands located at around 350 and 376 nm respectively, which suggests the formation of different luminescent centers. The emission color (Fig. 7b, d) is either in blue (layered ZnAc containing

samples) or green spectral domain (ZnO containing samples). It is known that the luminescence of samples depends both on the morphology and phase composition. Many reports show that the size variation of ZnO nanoparticles and the presence of defects have a strong influence on optical properties [45, 46]. ZnO needles and tetrapods exhibit mostly UV emission, while ZnO ribbons/combs nanostructures demonstrate a strong PL emission in the visible range. In our case, it is observed that the luminescent properties are mostly affected by the phase composition than the morphology of the particles. In addition, the emission intensities vary due to the contribution of multiple deep levels defects found in ZnO samples [47, 48].

ZnAc layered samples (Z4, Z5, Z6) exhibit higher emission in blue spectral domain (440, 473 nm) with an extension toward green zone (548 nm). Z12 presents the lowest emission intensity, which extends in both blue and green region due to structural inhomogeneity. Generally, in semiconductor materials, the most prominent emission (near band emission-NBE) is attributed to electron move from the bottom edge of the conduction band (CB), to the top edge of the valence band (VB) and is located in UV domain. On the other hand, the presence of various defects within the bandgap are responsible for emission in the visible spectral domain. The emission spectra under different excitation radiation of pure ZnO (Z11) and ZnO- $Zn(OH)_2$ sample (Z7) are presented in Fig. 8.

The NBE at 311 nm (3.98 eV), 337 nm (3.67 eV) and 383 nm (3.24 eV) attributed to free excitons recombination, are well distinguished under higher energy excitation (220, 258 nm) while the broad structured green emission at 550 nm (2.25 eV) due to defect states appears only under 352 nm excitation. The broadness of the emission peaks are the results of various bands overlapping coming from more than one deep level defects.

As depicted in Fig. 9, the deconvolution of the emission spectra for these two representative samples reveals the

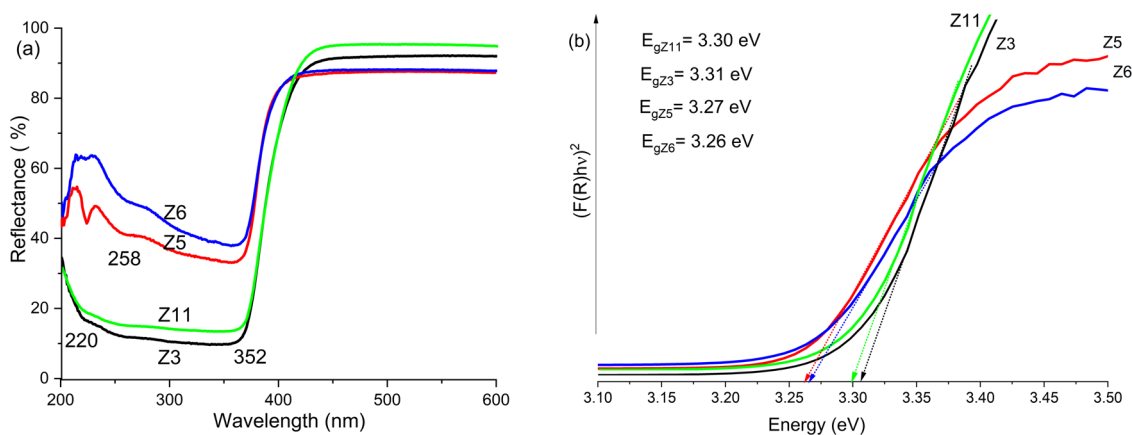


Fig. 6 UV-vis reflectance spectra (a) and Kubelka–Munk plots (b) of some representative ZnO samples

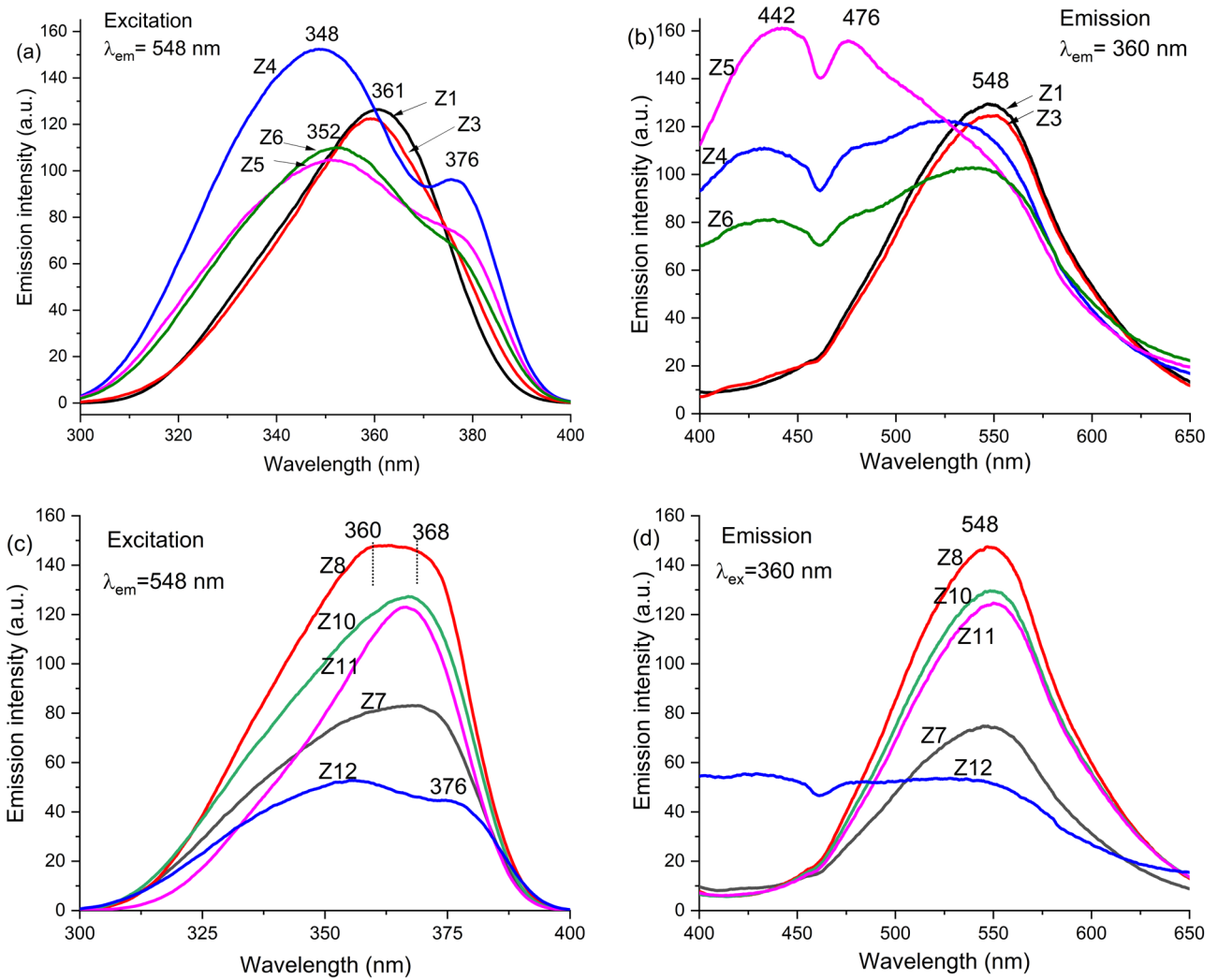


Fig. 7 Excitation (a, c) and emission (b, d) spectra of zinc oxide samples prepared in different synthesis conditions

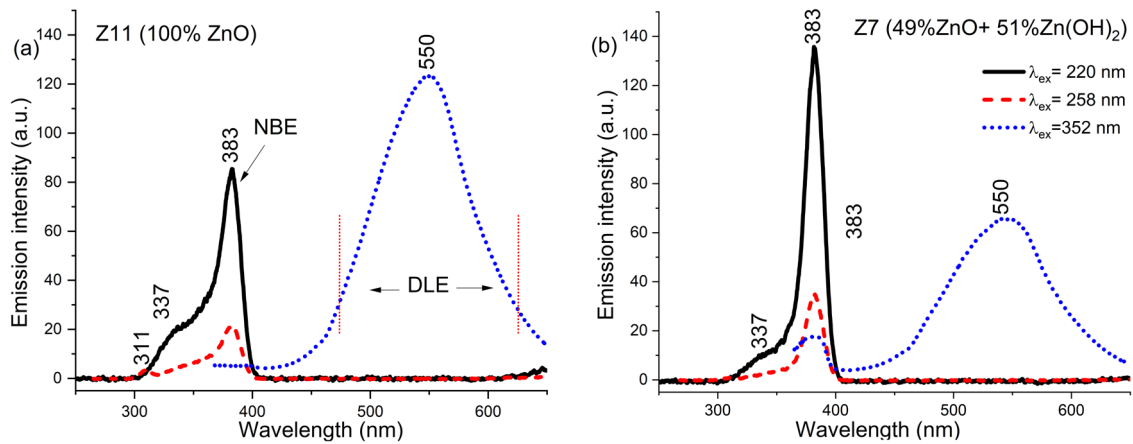


Fig. 8 Emission spectra of Z11 (a) and Z7 (b) under different excitation radiation

presence of multiple sub-bands situated in green domain (528, 549, 556 nm), blue (431, 479 nm) and red (610 nm) domain. The emission of pure ZnO (Z11) is located mainly in green domain, while for a layered structure (S15) the spectrum is much more complex with two main emissions sub-bands distinguished in blue region at 431 nm as well as in green region at 549 nm.

Along with these main sub-bands, several other smaller bands appear, mainly in the green domain. The origin of ZnO luminescence is extremely complex and intensely debated by researchers. As result of numerous studies, a consensus has been reached regarding the participation of different intrinsic defects in the ZnO luminescence [49–52]. There are three different types of intrinsic defect which may generate discrete electronic states between conduction and valence band, such as: missing atoms at regular lattice positions (zinc and oxygen vacancies), interstitials (zinc atoms occupying interstices in the lattice), anti-sites (Zn atom occupying O lattice site or vice versa) [49–52]. Oxygen vacancy (V_O) is a deep donor near or above CB, that give rise to green luminescence via a recombination process with photo-generated holes. Also, the literature reveals, other defects related to different impurities (i.e. Li, N, Si, Cu, C) in ZnO, which may contribute to the green emission [53].

V_O defects are often found to coexist with the interstitial oxygen (O_i). In this particular case, the experimental PL emission is in green–yellow range [54]. According to PL spectrum (Fig. 9b), the green emission of pure ZnO samples implies oxygen vacancies present in either neutral (V_O) or doubly charged state (V_O^{2-}). This phenomenon is described in other studies [55]. Because singly ionized oxygen vacancy (V_O^-), is thermodynamically unstable its participation may occur only under extensive light excitation [46]. Several studies mention that the yellow emission in ZnO is attributed to the presence of zinc and / or interstitial oxygen [56, 57] Therefore, the sub-band at 585 nm is related to O_i . The purple-blue band at 430 nm, seen for layered structure (Fig. 9a), implies transitions from interstitial zinc (Zn_i) to VB. Based on the calculations of Zhang [51] the defect level of V_O lies 0.9 eV above the valence band therefore, the blue band at 479 nm may indicate the contribution of electronic transitions from interstitial zinc (Zn_i) to the zinc vacancy (V_{Zn}) while the orange band at 610 nm is assigned to transition from Zn_i to O_i . The defect states and possible transitions responsible for ZnO luminescence are depicted in Fig. 9c. Several other surface defects can contribute to the luminescence due to hydroxyl groups [58].

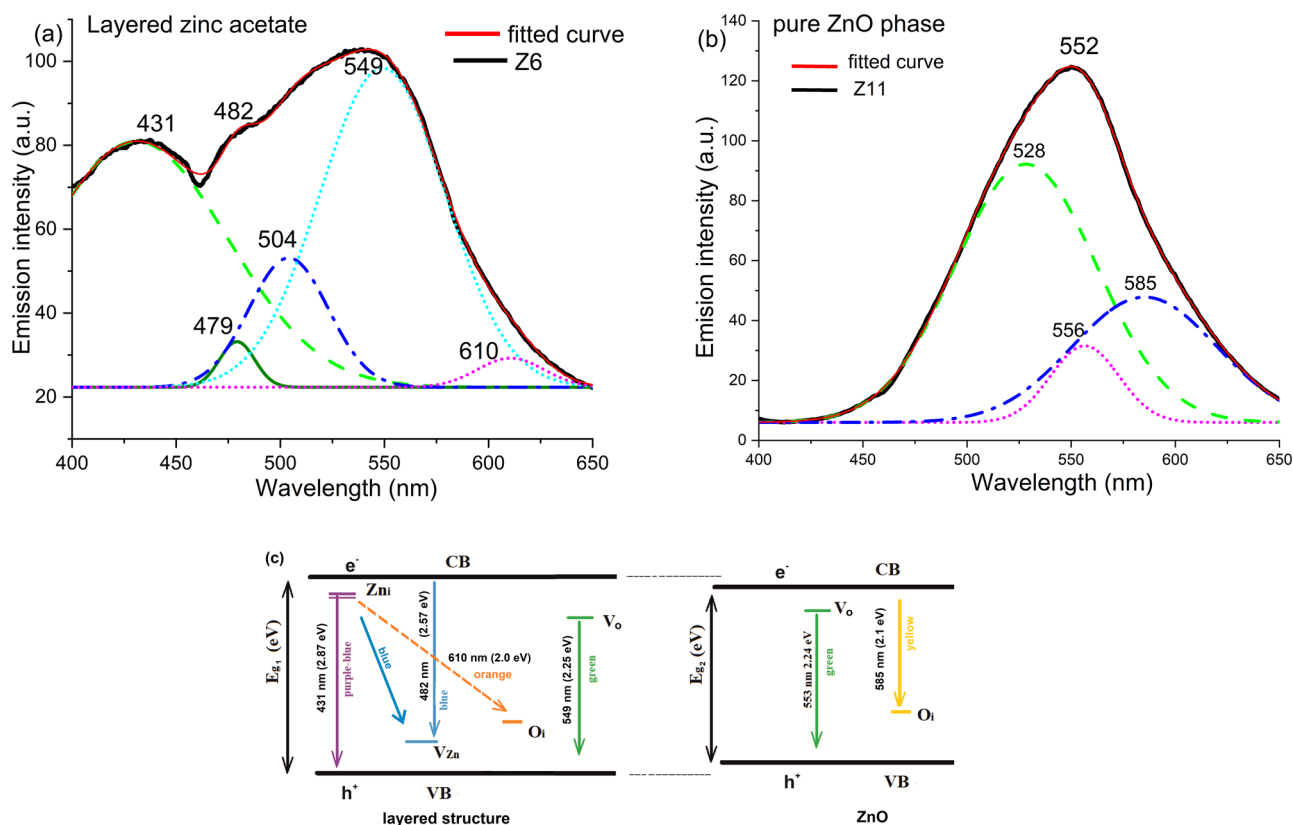


Fig. 9 Deconvoluted PL spectra obtained for Z6 (a), Z11 (b) samples and scheme of possible transitions (c)

4 Conclusions

Different varieties of ZnO nanoparticles were prepared at room temperature, without additives using DIA as precipitating agent by changing the molar ratio, the volume and the flow rate of the reactants. The precipitation performed in a slightly acidic media (DIA:Zn \leq 2) conduce to zinc acetate with layered structures. An high excess of DIA (DIA:Zn=10) abruptly increase the pH up to 11.5, leading to ZnO–Zn(OH)₂ mixtures. In order to obtain pure ZnO, the most convenient DIA:Zn molar ratio is 3. For large batches synthesis, the increase of reagent flow from 18 mL/min to 90 ml/min is mandatory to obtain pure ZnO. The smallest crystallite sizes (~25 nm) were obtained for pure ZnO samples. The structural model for (Zn₅(OH)₈(CH₃COO)₂ · 2H₂O) layered structure was proposed by DFT, using Zn₅(OH)₈(NO₃)₂ · 2H₂O structure as starting point. The calculated unit cell possesses two d_{Zn-Zn} = 13.3 Å gaps between the three layers of Zn chains, and the computed XRD pattern match well with the experimental one. The color extinction phenomenon observed in MOM as brown-orange (ZnO); yellow (Zn(OH)₂) and pale yellow with bright spots (layered ZnAc) correlates well with XRD structural phases. Depending on the synthesis conditions, various morphologies were identified: triangular (200–625 nm); rounded (100–650 nm), tetragonal bipyramids (~4.5 μm) and lamellar aggregates (150 nm–2 μm size, 30–150 nm thickness). Optimized pure ZnO consist of rounded nanoparticles of ~130 nm. The luminescence is either in blue (layered ZnAc containing samples) or green spectral domain (ZnO containing samples) due to interstitial zinc (Zni) and oxygen vacancy (V_O) defects.

Supplementary information The online version contains supplementary material available at <https://doi.org/10.1007/s10971-024-06313-z>.

Authors contributions All authors contributed to the study conception and design. Material preparation, data collection and analysis were performed by L.E. Muresan, I. Perhaita, A. M. V. Branzanic, C. Sarosi, L. Barbu-Tudoran, G. Borodi, I. Petean. The first draft of the manuscript was written by L.E. Muresan and all authors commented on previous versions of the manuscript. All authors read and approved the final manuscript.

Funding This work was supported by a grant of the Ministry of Research, Innovation and Digitization, CCCDI - UEFISCDI, project number PN-III-P2-2.1-PED-2021-2421, within PNCDI III and from the Romanian Ministry of Education and Research, PN-III-P1-1.1-PD-2021-0279 is gratefully acknowledged. The maintenance for the diffractometer was supported by the Ministry of Research, Innovation, and Digitization through Programme 1-Development of the National Research and Development System, Subprogramme 1.2-Institutional Performance-Funding Projects for Excellence in RDI, Contract No. 37PFE/30.12.2021.

Compliance with ethical standards

Conflict of interest The authors declare no competing interests.

References

- Kafle BP (2019) Chemical Analysis and Material Characterization by Spectrophotometry. Elsevier, ISBN 978-0-12-814866-2, 147. <https://doi.org/10.1016/C2017-0-02426-6>
- Zahoor R, Jalil A, Ilyas SZ, Ahmed S, Hassan A (2021) Optoelectronic and solar cell applications of ZnO nanostructures. Results Surf Interfaces 2:100003. <https://doi.org/10.1016/j.rsurfi.2021.100003>
- Baro B, Khimhun S, Das U, Bayan S (2023) ZnO based triboelectric nanogenerator on textile platform for wearable sweat sensing application. Nano Energy 108:108212. <https://doi.org/10.1016/j.nanoen.2023.108212>
- Zhang L, Shi C, Lu H, Li H, Zhou X, Wang Z, Ma J (2022) Porous cellulose gel-regulated flower-like ZnO-Cu nanoparticles for enhancing interfacial catalysis activity and recyclability in environmental catalysis. Appl Surf Sci 597:153737. <https://doi.org/10.1016/j.apsusc.2022.153737>
- Yadav A, Mondal K, Gupta A (2022) Metal Oxides for Biomedical and Biosensor Applications. Elsevier, Idaho Falls, United States, p 407. Kunal Mondal ed,
- Verma R, Pathak S, Srivastava AK, Prawer S, Tomljenovic-Hanic S (2021) ZnO nanomaterials: Green synthesis, toxicity evaluation and new insights in biomedical applications. J Alloy Compd 876:160175. <https://doi.org/10.1016/j.jallcom.2021.160175>
- Jiang Z, Liu B, Yu L, Tong Y, Yan M, Zhang R, Han W, Hao Y, Shangguan L, Zhang S, Li W (2023) Research progresses in preparation methods and applications of zinc oxide nanoparticles. J Alloy Compd 956:170316. <https://doi.org/10.1016/j.jallcom.2023.170316>
- Singh P, Singh RK, Kumar R (2021) Journey of ZnO quantum dots from undoped to rare-earth and transition metal-doped and their applications. RSC Adv 11:2512–2545. <https://doi.org/10.1039/d0ra08670c>
- Rajan S, Venugopal A, Kozhikkalathil H, Valappil S, Kale M, Mann M, Ahuja P, Munjal S (2023) Synthesis of ZnO nanoparticles by precipitation method: Characterizations and applications in decipherment of latent fingerprints. Mater Today: Proceedings. <https://doi.org/10.1016/j.matpr.2023.05.680>
- Majid F, Bashir M, Bibi I, Raza A, Ezzine S, Alwadai N, Iqbal M (2022) ZnO nanofibers fabrication by hydrothermal route and effect of reaction time on dielectric, structural and optical properties. J Mater Res Technol 18:4019–4029. <https://doi.org/10.1016/j.jmrt.2022.04.001>
- Al-luhaibi AA, Sendi RK (2022) Synthesis, potential of hydrogen activity, biological and chemical stability of zinc oxide nanoparticle preparation by sol-gel: A review. J Radiat Res Appl Sci 15:38–254. <https://doi.org/10.1016/j.jrras.2022.07.008>
- Shu Y, Duan X, Niu Q, Xie R, Zhang P, Pan Y, Ma Z (2021) Mechanochemical Alkali-Metal-Salt-mediated synthesis of ZnO nanocrystals with abundant oxygen Vacancies: An efficient support for Pd-based catalyst. Chem Eng J 426:131757. <https://doi.org/10.1016/j.cej.2021.131757>
- Kem A, Pasupuleti KS, Jayasimhadri M, Kim MD, Peta KR (2023) Core shell heterojunction interface in green synthesized Sm³⁺ ions doped ZnO nano-particles to promote the charge separation for efficient photocatalytic applications. J Alloy Compd 960:170841. <https://doi.org/10.1016/j.jallcom.2023.170841>
- Król A, Pomastowski P, Rafińska K, Railean-Plugaru V, Buszewski B (2017) Zinc oxide nanoparticles: Synthesis, antiseptic activity and toxicity mechanism. Adv Colloid Interface Sci 249:37–52. <https://doi.org/10.1016/j.cis.2017.07.033>
- Adama RE, Pozinab G, Willandera M, Nura O (2018) Synthesis of ZnO nanoparticles by co-precipitation method for solar driven photodegradation of Congo red dye at different pH. Photonics

- Nanostruct – Fundam Appl 32:11–18. <https://doi.org/10.1016/j.photonics.2018.08.005>
16. Verma RK, Nagar V, Aseri V, Mavry B, Pandit PP, Chopade RL, Singh A, Singh A, Yadav VK, Pandey K, Sankhla MS (2022) Zinc oxide (ZnO) nanoparticles: Synthesis properties and their forensic applications in latent fingerprints development. *Mater Today: Proc* 69:36–41. <https://doi.org/10.1016/j.matpr.2022.08.074>
 17. Goswami M, Adhikary NC, Bhattacharjee S (2018) Effect of annealing temperatures on the structural and optical properties of zinc oxide nanoparticles prepared by chemical precipitation method. *Optik* 158:1006–1015. <https://doi.org/10.1016/j.ijleo.2017.12.174>
 18. Kubiak A, Żółtowska S, Gabała E, Szybowicz M, Siwińska-Ciesielczyk K, Jesionowski T (2021) Controlled microwave-assisted and pH-affected growth of ZnO structures and their photocatalytic performance. *Powder Technol* 386:221–235. <https://doi.org/10.1016/j.powtec.2021.03.051>
 19. Lal M, Sharma P, Singh L, Ram C (2023) Photocatalytic degradation of hazardous Rhodamine B dye using sol-gel mediated ultrasonic hydrothermal synthesized of ZnO, nanoparticles. *Results Eng* 17:100890. <https://doi.org/10.1016/j.rineng.2023.100890>
 20. Liu L, Wang S, Liu W, Wang J, Zhang B, Yang J, Liu H, Li Y (2023) Supercritical hydrothermal synthesis of nano-ZnO: Effects of key parameters and reaction mechanism. *Ceram Int* 49:31313–3132. <https://doi.org/10.1016/j.ceramint.2023.07.079>
 21. Ungula J, Dejene BF, Swart HC (2018) Effect of pH on the structural, optical and morphological properties of Ga-doped ZnO nanoparticles by reflux precipitation method. *Phys B* 535:251–257. <https://doi.org/10.1016/j.physb.2017.07.052>
 22. Rezaei A, Katouei-zadeh E, Zebarjad SM (2022) Investigation of the parameters affecting the morphology of zinc oxide (ZnO) nanoparticles synthesized by precipitation method. *Mater Today Chem* 26:101239. <https://doi.org/10.1016/j.mtchem.2022.101239>
 23. Belcovi A, Fort CI, Mureşan LE, Perhaiţa I, Borodi G, Turdean GL (2023) Zinc oxide nanostructured platform for electrochemical detection of heavy metals. *Electroanalysis* 35:202200395. <https://doi.org/10.1002/elan.202200395>
 24. Perdew JP, Burke K, Ernzerhof M (1996) Generalized Gradient Approximation Made Simple. *Phys Rev Lett* 77(18):3865. <https://doi.org/10.1103/PhysRevLett.77.3865>
 25. Delley B (1990) An all-electron numerical method for solving the local density functional for polyatomic molecules. *J Chem Phys* 92(17):508. <https://doi.org/10.1063/1.458452>
 26. Grimme S, Antony J, Ehrlich S, Krieg H (2010) A consistent and accurate ab initio parametrization of density functional dispersion correction (DFT-D) for the 94 elements H-Pu. *J Chem Phys* 132. <https://doi.org/10.1063/1.3382344>
 27. Delley B (2000) From molecules to solids with the DMol3 approach. *J Chem Phys* 113(64):7756. <https://doi.org/10.1063/1.1316015>
 28. Dassault Systèmes BIOVIA (2017) Materials Studio, San Diego
 29. Alias SS, Ismail AB, Mohamad AA (2010) Effect of pH on ZnO nanoparticle properties synthesized by sol-gel centrifugation. *J Alloy Compd* 499:231–237. <https://doi.org/10.1016/j.jallcom.2010.03.174>
 30. Samaele N, Amornpitoksuk P, Suwanboon S (2010) Effect of pH on the morphology and optical properties of modified ZnO particles by SDS via a precipitation method. *Powder Technol* 203:243–247. <https://doi.org/10.1016/j.powtec.2010.05.014>
 31. Hosono E, Fujihara S, Kimura T, Imai H (2004) Growth of layered basic zinc acetate in methanolic solutions and its pyrolytic transformation into porous zinc oxide films. *J Colloid Interface Sci* 272:391–398. <https://doi.org/10.1016/j.jcis.2003.10.005>
 32. Biswick T, Jones W, Pacula A, Serwicka E, Podobinski J (2009) Evidence for the formation of anhydrous zinc acetate and acetic anhydride during the thermal degradation of zinc hydroxy acetate, $Zn_5(OH)_8(CH_3CO_2)_2 \cdot 4H_2O$ to ZnO. *Solid State Sci* 11:330–335. <https://doi.org/10.1016/j.solidstatesciences.2008.06.018>
 33. Snyder RL (1992) The Use of Reference Intensity Ratios in X-Ray Quantitative Analysis. *Powder Diffr* 7(4):186–193. <https://doi.org/10.1017/S0885715600018686>
 34. Music S, Dragecic D, Popovic S (2007) Influence of synthesis route on the formation of ZnO particles and their morphologies. *J Alloy Compd* 429:242–249. <https://doi.org/10.1016/j.jallcom.2006.03.084>
 35. Stahlin W, Oswald HR (1970) The Crystal Structure of Zinc Hydroxide Nitrate, $Zn_5(OH)_8(NO_3)_2 \cdot 2H_2O$. *Acta Cryst B* 26:860. <https://doi.org/10.1107/S0567740870003230>
 36. Ghotbi MY (2010) Synthesis and characterization of nano-sized ϵ -Zn(OH)₂ and its decomposed product, nano-zinc oxide. *J Alloy Compd* 491:420–422. <https://doi.org/10.1016/j.jallcom.2009.10.214>
 37. Saroj SK, Pal S, Nagarajan R (2020) Polyol intercalation in copper substituted zinc hydroxide acetate and evaluation of its adsorptive role towards Congo red dye. *Appl Clay Sci* 185:105411. <https://doi.org/10.1016/j.clay.2019.105411>
 38. Jain A, Ong SP, Hautier G, Chen W, Richards WD, Dacek S, Cholia S, Gunter D, Skinner D, Ceder G, Persson KA (2013) The Materials Project: A materials genome approach to accelerating materials innovation. *APL Mater* 1(1):011002
 39. He Y, Li H, Qian W, Wu Y (2023) High-resolution light field imaging based on liquid crystal microlens arrays with ZnO microstructure orientation. *Opt Lasers Eng* 162:107424. <https://doi.org/10.1016/j.optlaseng.2022.107424>
 40. Yu G, Cheng Y (2020) Effects of Inorganic ZnO Particle Doping on Crystalline Polymer Morphology and Space Charge Behavior. *Coatings* 10:932. <https://doi.org/10.3390/coatings10100932>
 41. Dombrowski RT (2013) Microscopy techniques for analyzing the phase nature and morphology of biomaterials. Jaffe M, Hammond W, Toliás P, Arinze T, ed, Woodhead Publishing Series in Biomaterials. 1-33. <https://doi.org/10.1533/9780857093684.1>
 42. Escobedo-Morales A, Ruiz-Lopez II, deL Ruiz-Peralta M, Tepech-Carrillo L, Sanchez-Cantu M, Moreno-Orea JE (2019) Automated method for the determination of the band gap energy of pure and mixed powder samples using diffuse reflectance spectroscopy. *Heliyon* 5:e01505. <https://doi.org/10.1016/j.heliyon.2019.e01505>
 43. Islam SMZ, Gayen T, Moussawi A, Shi L, Seredych M, Bandoz TJ, Alfano R (2013) Structural and optical characterization of Zn(OH)₂ and its composites with graphite oxides. *Opt Lett* 38(6):962–964. <https://doi.org/10.1364/OL.38.000962>
 44. Kamarulzaman N, Kasim MF, Rusdi R (2015) Band Gap Narrowing and Widening of ZnO Nanostructures and Doped Materials. *Nanoscale Res Lett* 10:346. <https://doi.org/10.1186/s11671-015-1034-9>
 45. Wang J, Chen R, Xiang L, Komarnenic S (2018) Synthesis, properties and applications of ZnO nanomaterials with oxygen vacancies: A review. *Ceram Int* 44:7357–7377. <https://doi.org/10.1016/j.ceramint.2018.02.013>
 46. Gurylev V, Perng TP (2021) Defect engineering of ZnO: Review on oxygen and zinc vacancies. *J Eur Ceram* 41:4977–4996. <https://doi.org/10.1016/j.jeurceramsoc.2021.03.031>
 47. Banerjee D, Kar AK (2019) Effect of hydroxide ion concentration on the evolution of nanostructures and structure correlated luminescence of ZnO nanopowders. *Opt Mater* 89:430–440. <https://doi.org/10.1016/j.optmat.2019.01.048>
 48. Qutes FJ, Germino JC, Atvars TDZ (2014) Improvement in the emission properties of a luminescent anionic dye intercalated between the lamellae of zinc hydroxide-layered. *Colloids Surf A Physicochem Eng Asp* 459:194–201. <https://doi.org/10.1016/j.colsurfa.2014.07.009>

49. Nadupalli S, Repp S, Weber S, Erdem E (2021) About defect phenomena in ZnO nanocrystals. *Nanoscale* 13:9160–9171. <https://doi.org/10.1039/d1nr00943e>
50. Ellmer K, Bikowski A (2016) Intrinsic and extrinsic doping of ZnO and ZnO alloys. *J Phys D: Appl Phys* 49:413002. <https://doi.org/10.1088/0022-3727/49/41/413002>
51. Zhang SB, Wei SH, Zunger A (2001) Intrinsic n-type versus p-type doping asymmetry and the defect physics of ZnO. *Phys Rev B* 63:075205. <https://doi.org/10.1103/PhysRevB.63.075205>
52. Rai H, Prashant M, Kondal N (2022) A review on defect related emissions in undoped ZnO nanostructures. *Mater Today: Proc* 48:1320–1324. <https://doi.org/10.1016/j.matpr.2021.08.343>
53. Lv J, Li C, Chai Z (2019) Defect luminescence and its mediated physical properties in ZnO. *J Lumin* 208:225–23. <https://doi.org/10.1016/j.jlumin.2018.12.050>
54. Lv J, Fang M (2018) Photoluminescence study of interstitial oxygen defects in ZnO nanostructures. *Mater Lett* 218:18–21. <https://doi.org/10.1016/j.matlet.2018.01.137>
55. Gong Y, Andelman T, Neumark GF, O'Brien S, Kuskovsky IL (2007) Origin of defect-related green emission from ZnO nanoparticles: effect of surface modification. *Nanoscale Res Lett* 2:297–302. <https://doi.org/10.1007/s11671-007-9064-6>
56. Brahma S, Shivashankar SA (2016) Yellow–red luminescence in ZnO nanoparticles synthesized from zinc acetylacetonate phenanthroline. *Mater Lett* 164:235–238. <https://doi.org/10.1016/j.matlet.2015.10.147>
57. García-Velasco AC, Baez-Rodríguez A, Bizarro M, Calderon-Olvera RM, Hernandez-Torres J, García-Gonzalez L, Zamora-Peredo L (2022) Surface defect-rich ZnO nanostructures with high yellow-orange luminescence. *J Lumin* 25:119187. <https://doi.org/10.1016/j.jlumin.2022.119187>
58. Raoufi D (2013) Synthesis and photoluminescence characterization of ZnO nanoparticles. *J Lumin* 134:213–219. <https://doi.org/10.1016/j.jlumin.2012.08.045>

Publisher's note Springer Nature remains neutral with regard to jurisdictional claims in published maps and institutional affiliations.

Springer Nature or its licensor (e.g. a society or other partner) holds exclusive rights to this article under a publishing agreement with the author(s) or other rightsholder(s); author self-archiving of the accepted manuscript version of this article is solely governed by the terms of such publishing agreement and applicable law.